Journal of Sound and Vibration 537 (2022) 117144

Contents lists available at ScienceDirect

Journal of Sound and Vibration

journal homepage: www.elsevier.com/locate/jsvi

Experimental study of the dynamic stall noise on an oscillating airfoil

David Raus [a,*], Benjamin Cotté [a,*], Romain Monchaux [a], Emmanuel Jondeau [b], Pascal Souchotte [b], Michel Roger [b]

[a] Institute of Mechanical Sciences and Industrial Applications (IMSIA), ENSTA Paris, CNRS, CEA, EDF, Institut Polytechnique de Paris, France
[b] Laboratoire de Mécanique des Fluides et d'Acoustique, Université de Lyon, École Centrale de Lyon, F-69134 Écully, France

ARTICLE INFO

Keywords:
Airfoil noise
Pitching airfoil
Anechoic wind tunnel
Open rotor
Trailing-edge noise

ABSTRACT

In this paper, the noise emitted by an oscillating NACA0012 airfoil at Reynolds number $Re_c = 2.1 \times 10^5$ is studied. Combined far-field noise and surface pressure measurements are performed in order to investigate the effect of the amplitude of motion α_1 and reduced frequency k on the emitted far-field noise. These two parameters can be combined using the reduced pitch rate $k_\star = \alpha_1 k$ that is shown to be the most relevant parameter in this study. The dynamic stall noise is characterized by an increase of the noise amplitude at frequencies below 700 Hz and takes place each time the airfoil incidence increases over the critical dynamic stall angle. For a low reduced pitch rate ($k_\star = 1.2 \times 10^{-3}$), a quasi-steady regime is obtained, with the light-stall and deep-stall regimes commonly observed for a static airfoil taking place during the pitching motion. For a higher pitch rate ($k_\star = 13.1 \times 10^{-3}$), an increase of the duration and amplitude of the broadband noise occurring at the stall onset is identified. For all the reduced pitch rates investigated, a delay in the apparition of the stall noise is observed in comparison with the static stall noise, leading to a hysteresis of the stall noise as a function of the angle of attack.

1. Introduction

Dynamic stall is an unsteady phenomenon taking place when a lifting surface is oscillating over its critical stall angle of attack. This can be encountered on rotating machines such as helicopter propellers or horizontal-axis and vertical-axis wind turbine blades [1–3]. The aerodynamics of airfoils oscillating over the stall angle have been deeply studied over the years [1,4–6]. The dynamic stall is characterized by a lift overshoot and a delay in the boundary layer separation in comparison with the static stall, leading the lift coefficient to exhibit a hysteresis as a function of the angle of attack. The dynamic stall is associated with the generation and convection of the dynamic stall vortex. This vortex forms at the leading-edge of the airfoil and originates from the roll-up of the shear layer previously developing between the regions of reverse and free-stream flow [7]. After the dynamic vortex detaches and is convected over the airfoil suction side, the flow becomes fully separated over the suction side. This is associated with a drop of lift and pitching moment. The fully separated stage of the cycle continues until the flow reattaches for smaller angles of attack during the downstroke phase of the cycle.

These cyclic variations of the flow field around the airfoil can lead to cyclic variations of the generated far-field noise. The noise emitted by a static airfoil is known to strongly depend on its angle of attack [8,9]. On wind turbines, periodic modulations of few decibels of the broadband noise take place due to trailing-edge noise directivity and convective amplification [10]. This

* Corresponding authors.
E-mail addresses: david.raus@ensta-paris.fr (D. Raus), benjamin.cotte@ensta-paris.fr (B. Cotté).

https://doi.org/10.1016/j.jsv.2022.117144
Received 30 September 2021; Received in revised form 16 June 2022; Accepted 17 June 2022
Available online 21 June 2022

phenomenon is referred to as Normal Amplitude Modulation. Stronger variations of the emitted noise has been reported on wind turbines, referred to as Other Amplitude Modulation (OAM). The cause of this phenomenon is not determined but it is thought to originate from the periodic separation and stall of the blade during its revolution [10].

The noise generated by a static airfoil in stall conditions has been studied experimentally [2,8,9] and more recently computationally [11]. The stall noise is characterized by a broadband increase of the noise of more than 10 dB at low frequencies compared to the trailing-edge noise of an attached turbulent boundary layer [8]. Moreau et al. [9] studied the noise emitted by several airfoils near stall and in stall, at chord-based Reynolds number $Re_c = Uc/\nu = 1.5 \times 10^5$, with U, c and ν the free-stream velocity, the airfoil chord and the kinematic viscosity of air, respectively. The authors identified a light stall and a deep stall regime. The light stall regime is characterized by a high amplitude broadband noise between 100 Hz and 1000 Hz, while for very large angles of attack the deep stall regime is characterized by a diminution of the broadband noise amplitude, and the presence of a narrow-band peak that can originate from shear layer instabilities and large scale vortex shedding. Similar observations were made by Laratro et al. [12] with airfoils of various thicknesses at $Re_c = 0.96 \times 10^5$. The authors also showed that the transition from trailing-edge noise to stall noise is sharper as the thickness of the airfoil increases, and that the interaction between the vorticity shed from the leading and trailing edges and the airfoil can be responsible for the light stall noise. Bertagnolio et al. [2] conducted experiments with various airfoils at Reynolds numbers $1 \times 10^6 < Re_c < 6 \times 10^6$. The authors developed an empirical model for the surface pressure fluctuations and far-field noise spectra, by finding scaling laws for the convection velocity and chordwise and spanwise correlation lengths for stalled airfoils. Recently, Lacagnina et al. [13] studied the noise generated by a cambered NACA65-(12)10 airfoil at high angles of attack, thanks to combined far-field acoustic measurements and surface pressure, hot-wire and Particle Image Velocimetry (PIV) measurements, and propose an interpretation for the origin of the stall noise. According to the authors, the generation of the static stall noise can originate from the interaction between the shear layer (separating the free stream and the separated boundary layer region) and the suction side of the airfoil, thanks to three mechanisms: coherent structures convected in the detached shear layer, instabilities in the detached shear layer, and shear layer flapping. These three mechanisms can induce unsteady hydrodynamic pressure on the airfoil surface that can be scattered at the trailing edge and radiate to the far-field.

Unlike its static counterpart, the acoustic radiation of oscillating airfoils just recently started to be studied. The noise emitted by rigid or elastic oscillating thin airfoils was first studied analytically by using the Powell–Howe acoustic analogy [14]. The results show that, depending on the oscillating frequency, the elasticity of the airfoil can lead to an amplification or a decrease of the emitted far-field noise. Zhou et al. [15] studied experimentally the noise emitted by a symmetrical NACA0012 airfoil at low Reynolds number $Re_c = 6.6 \times 10^4$ and oscillating below the stall angle. The emitted noise appeared to vary periodically and in-phase with the oscillations, with the laminar vortex shedding noise appearing only for specific angles of attack of the pitching cycle. The noise emitted by and airfoil oscillating above the dynamic stall angle have been studied experimentally in two different facilities [16,17]. Experiments of Siegel et al. [16] were performed with a cambered NACA64-418 at $Re_c = 8 \times 10^5$ in an open wind-tunnel, in which PIV and far-field acoustic pressure measurements were correlated in order to identify the flow regions contributing the most to the emitted noise. These regions vary during the pitching motion and increase during the fully stalled phase of the cycle. Mayer et al. [17] conducted experiments in an aeroacoustic wind-tunnel with a Kevlar-walled test section, using a NACA0012 at $Re_c = 4.2 \times 10^5$. The emitted far-field noise amplitude appeared to increase as the oscillating frequency of the airfoil increased. Time–frequency analysis of the surface pressure fluctuations near the trailing-edge showed a strong increase of the spectral amplitude during the stalled stage of the cycle, that the authors attributed to the development and convection of the dynamic stall vortex.

These studies did not investigate how the far-field noise evolves throughout the airfoil pitching motion. The present research aims at describing the features of the noise emitted by a NACA0012 airfoil oscillating in dynamic stall conditions. Combined far-field and surface pressure measurements are performed in order to provide a better insight into the variations of the generated far-field noise during the oscillation. In order to investigate the differences between the static and dynamic stall noises, emphasis is placed on the effect of the frequency and amplitude of the oscillations on the resulting noise. Firstly, the experimental setup and the parameters of the investigated regimes are introduced in Section 2. Secondly, Section 3 describes the features of the stall noise for a static airfoil, and investigates the noise emitted by an oscillating airfoil, using phase-averaged time–frequency analysis and Overall Sound Pressure Level analysis. Finally, Sections 4 and 5 propose a discussion and concluding remarks on the experimental results.

2. Experimental setup and data acquisition

2.1. Description of the experimental setup

The experiments were performed in the anechoic wind tunnel of the Ecole Centrale de Lyon. This wind tunnel consists of an open jet with a rectangular 0.4 m × 0.3 m nozzle exit, enclosed in an anechoic chamber of dimensions 8 m × 9 m × 10 m, with a cut-off frequency below 100 Hz. Two horizontal end-plates are installed downstream of the nozzle exit in order to guide the incoming flow, as shown in Fig. 1(a). Brushes are added at the curved edge of these end-plates to mitigate the scattering of the plate-boundary layer into acoustic waves. Measurements were conducted on a vertical NACA0012 airfoil of chord $c = 0.12$ m and of span $s = 0.30$ m, the ends of which are clamped into disks that are integrated into the end-plates. The pitching motions of the airfoil are driven by a motor placed beneath the lower end-plate. The airfoil is centered on the disks so that it rotates about its center-chord. In order to force transition to turbulent boundary layers on the airfoil and to avoid the generation of the laminar boundary layer tonal noise at low incidence [8], the airfoil is tripped using of a 25 mm wide tape. The tape is placed between $x/c = 0.16$ and $x/c = 0.36$ on both sides of the airfoil, and covers its entire span.

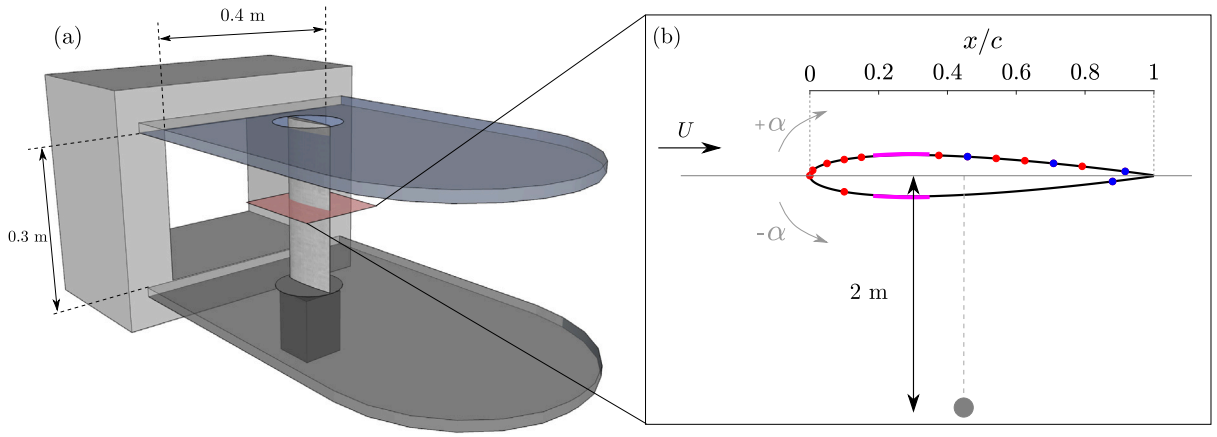

Fig. 1. Schematic of the experimental setup: (a) Nozzle exit (b) Positions of the measuring points. Red dots and blue dots show the positions where only the steady-state surface pressure is measured and the positions where both the steady and fluctuating wall pressures are measured, respectively. The gray dot shows the position of the far-field microphone. Purple areas show the positions of the tripping tape. Fig. 1b is not on scale. (For interpretation of the references to color in this figure legend, the reader is referred to the web version of this article.)

Table 1
Parameters associated with the six oscillating airfoil configurations.

Exp.	α_0 (°)	α_1 (°)	f_o (Hz)	k	$k_\star$
1	15	7	0.66	0.01	1.2 $\times 10^{-3}$
2	15	7	1.33	0.02	2.4 $\times 10^{-3}$
3	15	7	3.32	0.05	6.1 $\times 10^{-3}$
4	15	15	0.66	0.01	2.6 $\times 10^{-3}$
5	15	15	1.33	0.02	5.2 $\times 10^{-3}$
6	15	15	3.32	0.05	13.1 $\times 10^{-3}$

The airfoil was subjected to a flow of free-stream velocity $U = 25$ m/s, corresponding to a Reynolds number based on the chord $Re_c = 2.1 \times 10^5$ and to a Mach number $M_a = U/c_0 = 0.07$, with $c_0 = 343$ m/s the speed of sound. The turbulence intensity of the incoming flow as deduced from hot-wire measurements upstream of the airfoil is $u'_{rms}/U = 0.4\%$, with u'_{rms} the root mean square value of the velocity fluctuations at the airfoil mid-span height.

The airfoil was subjected to a sinusoidal variation of the angle of attack defined as:

$$\alpha_{d,g}(t) = \alpha_0 + \alpha_1 \sin(2\pi f_o t), \tag{1}$$

where α_0 is the mean angle of attack, α_1 is the amplitude of the motion and f_o is the oscillation frequency. In this paper, $\alpha_0 = 15°$, and $\alpha_1 = 7°$ or 15°. Three oscillation frequencies $f_o = 0.66$ Hz, 1.33 Hz and 3.32 Hz were tested, corresponding to reduced frequencies $k = \pi f_o c/U = 0.01$, 0.02 and 0.05. The reduced frequency k represents the ratio of time scales associated with the free-stream convection velocity of the flow and with the pitching motion of the airfoil . The flow is considered to be significantly unsteady for $k \geq 0.05$ [6]. For experiments with varying amplitude of motion α_1, the reduced frequency k can be insufficient to compare the observed regimes, as the aerodynamics of the airfoil depends on its pitch rate. Sheng et al. [18] therefore propose a reduced pitch rate $k_\star$, noted r_{eq} in their article. For oscillating airfoils, the reduced pitch rate is defined as the maximum of the instantaneous pitch rate of the sinusoidal motions $k_\star = \alpha_1 k$, with α_1 in radians. Experimental parameters and values of reduced pitch rate $k_\star$ are listed in Table 1. The boundary between quasi-steady and dynamic stall is estimated at $k_\star = 0.01$ for a NACA0012 [18], thus it appears on Table 1 that the 10 regimes studied here cover a range from quasi-steady stall to dynamic stall. Measurements with a static airfoil were also conducted, for static angles of attack $\alpha_{s,g}$ increased from 0° to 30° with increments of 3° between measurements. Note that measurements with a static airfoil are only conducted for increasing angle of attack $\alpha_{s,g}$.

2.2. Open-jet wind tunnel corrections

The subscript g in both static and dynamic angles of attack refers to the geometrical angle of attack. The latter is defined as the angle between the nozzle exit axis and the airfoil chord, as shown in Fig. 1. In an open-jet wind tunnel, the flow deviates from the nozzle axis, reducing the effective angle of attack and lift coefficient of the airfoil. For a static airfoil, corrections schemes were developed based on the method of images in order to estimate the effective angle of attack $\alpha_{s,e}$. Two corrections commonly used for static airfoils are tested here. According to Brooks et al. [19], the angle of attack of an airfoil in an unbounded flow giving the same lift as the airfoil in the wind tunnel can be estimated as:

$$\alpha_{s,e} = \frac{\alpha_{s,g}}{\eta}, \tag{2}$$

Table 2
Geometric and effective static angles of attack investigated for a static airfoil considering the corrections of Brooks et al. [19] and of Garner et al. [20].

$\alpha_{s,g}(°)$	0	3	6	9	12	15	18	21	24	27	30
$\alpha_{s,e}(°)$ - Brooks	0	1.9	3.9	5.8	7.8	9.7	11.6	13.6	15.5	17.5	19.4
$\alpha_{s,e}(°)$ - Garner	0	1.9	3.8	6.0	8.4	12.4	15.4	18.1	20.9	23.6	26.0

where $\eta = (1+2\sigma)^2 + \sqrt{12\sigma} \simeq 1.55$, $\sigma = (\pi^2/48)(c/W)^2$ and $W = 0.4$ m is the nozzle exit width. The other tested corrections originates from the work of Garner et al. [20], who obtain:

$$\alpha_{s,e} = \alpha_{s,g} - \frac{1}{2\pi}\left(\frac{L_0}{L} - 1\right) C_l, \tag{3}$$

$$C_{l,\mathrm{corr}} = C_l + C_l \frac{\pi^2}{24}\left(\frac{c}{\beta W}\right)^2, \tag{4}$$

$$\beta = \sqrt{|1 - Ma^2|} \simeq 1, \tag{5}$$

where C_l and $C_{l,\mathrm{corr}}$ are the measured and corrected lift coefficients, respectively, and L_0/L is a function of the chord and nozzle exit width [20]. The effective angle of attack values obtained with these corrections are given in Table 2.

These incidence corrections have not been tested nor validated experimentally for an oscillating airfoil configuration yet. For an oscillating airfoil, it is likely that the deflection of the flow adapt to the angle of attack with a time-lag, and that angle of attack corrections should be depending on the reduced frequency of the oscillation. To the authors' knowledge, such corrections have not yet been developed and it is not the aim of this article to develop such corrections. Geometrical angles of attack α_g are thus used in the following. The reader can refer to Table 2 to estimate the effective angle of attack of the airfoil.

2.3. Surface pressure and acoustic measurements

Measurements of the steady wall pressure on the airfoil are performed using 14 steady pressure taps at a sampling frequency $f_s = 100$ Hz, installed mid-span along the chord of the airfoil (see Fig. 1(b)), and connected by a tubing system to a Kulite KMPS-1-64 pressure scanner. It is noteworthy that the steady pressure taps are mainly distributed on one side of the airfoil. In order to estimate the lift and moment coefficients of the airfoil by integrating the steady pressure along its two sides, it is therefore necessary to conduct experiments for both positive and negative angles of attack of the airfoil, so that the pressure taps are alternatively located on its suction and pressure sides. For a given static configuration, measurements are thus performed for $\alpha_{s,g}$ and $-\alpha_{s,g}$, the sign of the angle of attack being defined in Fig. 1(b). For dynamic configurations, measurements are performed for $\alpha_{d,g} = \alpha_0 + \alpha_1 \sin(2\pi f_o t)$ and $\alpha_{d,g} = -\alpha_0 + \alpha_1 \sin(2\pi f_o t)$, and post-synchronized during post-processing as explained hereafter.

The surface pressure fluctuations are measured by four Remote-Microphone Probes (RMP), located at four of the steady pressure tap positions (see Fig. 1(b)). The RMPs are equipped with Brüel & Kjær 4958 type microphones, and the signal acquisition is made at a sampling frequency $f_s = 51.2$ kHz. The RMP dynamic response measurement and calibration method used here is described in Ref. [21].

The far-field noise is investigated with the same sampling frequency using a GRAS 46BE microphone, placed in the mid-span plane, 2 meters away from the airfoil center-chord and normal to the incoming flow direction (see Fig. 1(b)). This is relevant for two reasons. Firstly, airfoil noise is of dipolar nature with equivalent dipoles oriented normal to the surface. The mid-span plane, far-field positioning prevents from significant reflection and scattering by the supporting plates. Secondly, at the low frequencies for which stall noise is dominant, the airfoil chord is compact and the expected directivity reduces to that of a point lift dipole. Keeping the microphone stationary during the oscillatory motion of the airfoil does not result in significant changes because the directivity lobe is very wide. The acquisitions of the four remote microphone probes and of the far-field microphone are synchronized with the acquisition of the instantaneous angle of attack of the airfoil. The steady pressure taps measurements are synchronized with the microphones in the post-processing phase by comparing the signals of a steady pressure tap and of a remote microphone probe located at the same chord position. Background noise is measured by removing the airfoil and blowing at the same speed. It is assumed to be uncorrelated to the airfoil noise. However, for high incidences the background noise may be modified at low frequencies by the presence of the airfoil, due to interactions between the airfoil and the shear layers of the nozzle jet [9].

2.4. Data acquisition and processing

For the static airfoil configurations, the far-field noise and surface pressure signals are measured for a period of 30 s. The Power Spectral Density (PSD) of the signals is calculated using the Welch's method [22], with a Hamming window size of 6400 samples and 50% overlap. The resulting PSD have a frequency resolution of 8 Hz.

For the oscillating airfoil regimes, the far-field noise and surface pressure signals are measured for a period of 100 periods, the 10 first periods being discarded from the analysis to avoid transient effects. The calculation of the spectrograms is performed by using a short-time Fourier transform of the pressure signals. The signals are divided into overlapping windowed segments, and the spectrograms show an estimate of the Power Spectral Density (PSD) on each segments. Two types of spectrograms are computed.

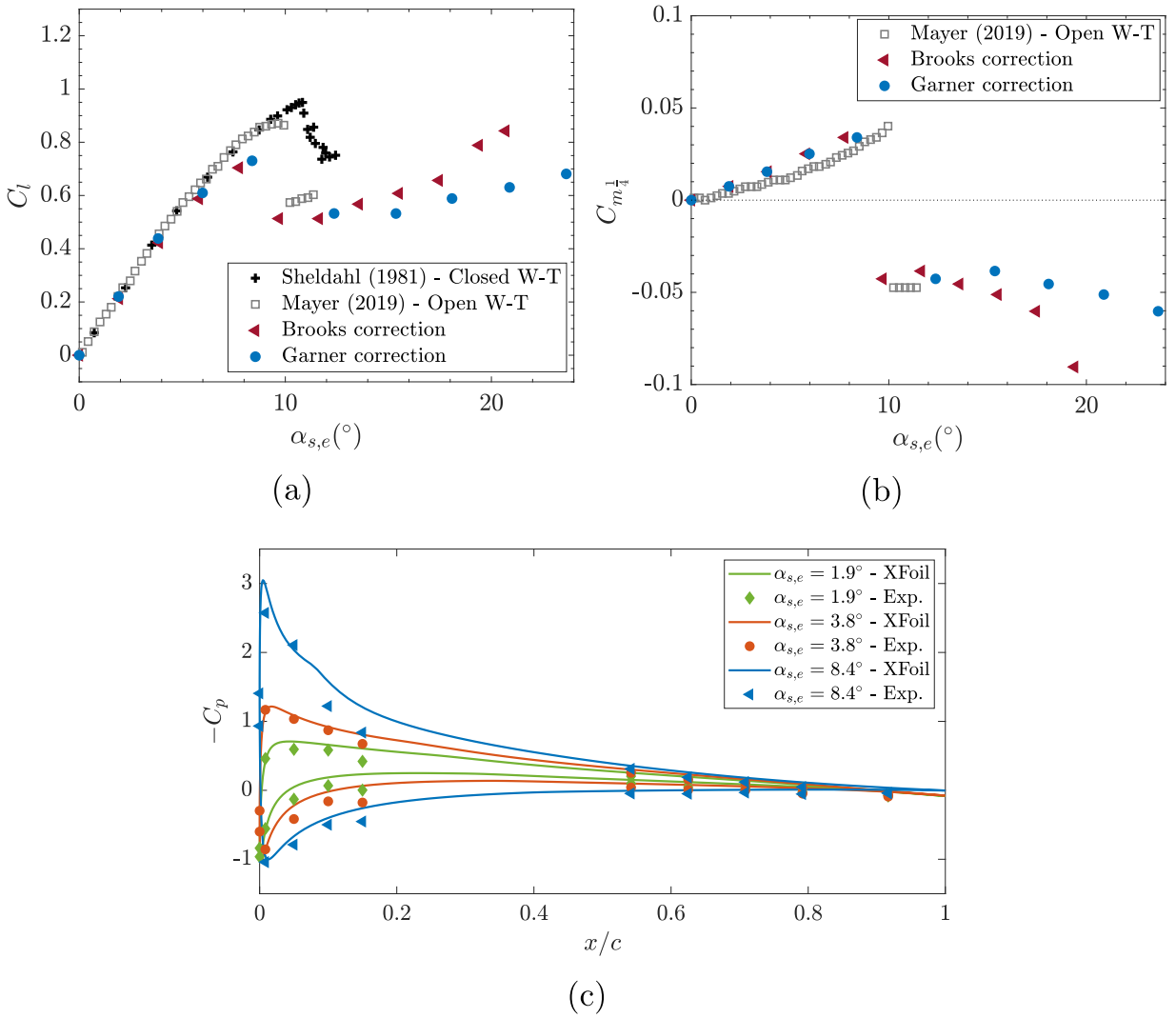

Fig. 2. Comparison of the (a) lift coefficient and (b) moment coefficient at the quarter chord as functions of the effective static angle of attack $\alpha_{s,e}$ calculated with corrections by [19,20]. Open wind tunnel data of [23] are corrected with Brooks' correction, with $\eta = 1.73$. (c) Comparison of static pressure distribution $-C_p$ between experiments and XFoil simulations for effective angles of attack estimated with Garner corrections.

In order to represent the microphone signals in the time–frequency domain, a high-pass filter with a cut-off frequency of 50 Hz is applied to the signals to remove contamination by the background noise. Spectrograms are then computed with 80% overlap and window sizes of 7000 samples, 3500 samples and 1400 samples for $f_0 = 0.66$ Hz, $f_0 = 1.33$ Hz and $f_0 = 3.32$ Hz, respectively, in order to have the same number of windows per cycle and the same angle of attack resolution for every oscillation frequency. Segments are extended to 8192 samples using zero-padding to obtain the same frequency resolution for every oscillation frequency. The resulting spectrograms have a frequency resolution of 6.25 Hz, and time resolutions of 27 ms, 14 ms and 6 ms, respectively. For the frequency-integrated spectrograms and Overall Sound Pressure calculation, spectrograms are computed with window sizes of 1400 samples and 80% overlap for every oscillation frequencies, in order to improve the time resolution. The resulting frequency and time resolutions are 37 Hz and of 6 ms.

3. Experimental results

3.1. Reference case: the static airfoil stall noise

As a reference case, the aerodynamics and broadband noise radiation of a static airfoil are first investigated. The lift coefficient C_l and the moment coefficient at the quarter chord $C_{m\frac{1}{4}}$ are estimated by integrating the steady surface pressure along the airfoil chord and are presented in Fig. 2. The static stall angle α_{ss} is identified as the angle of lift drop and sign inversion of the moment

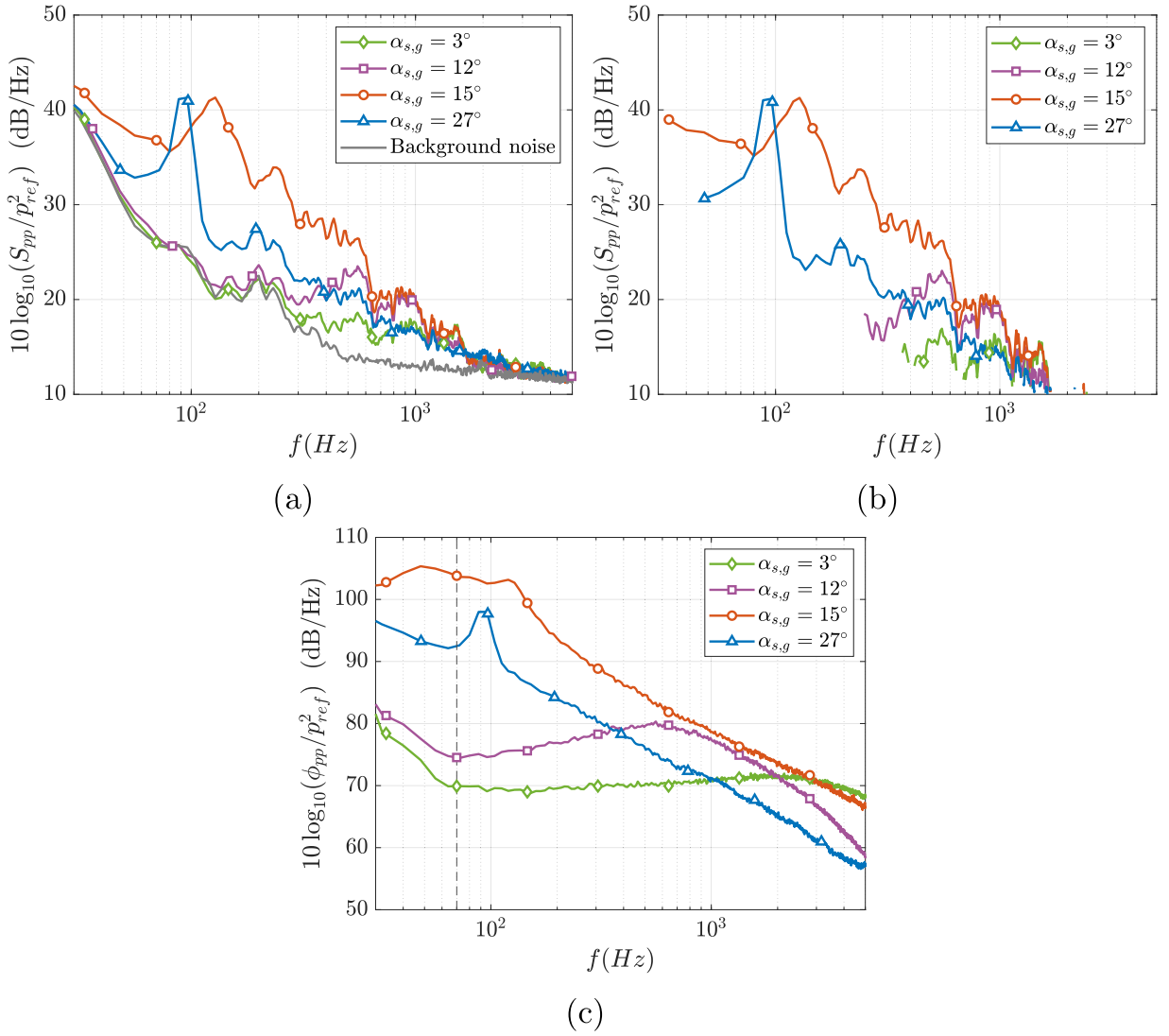

Fig. 3. PSD of the far-field acoustic pressure for various static angles of attack: (a) raw spectra (b) with background noise subtracted and data discarded if the total noise does not exceeds the background noise by at least 2 dB. (c) PSD of the surface pressure fluctuations at $x/c = 0.92$ on the suction side of the airfoil, for various static angles of attack. The vertical dashed black line shows the limit below which the surface pressure spectra is thought to be contaminated by the wind tunnel background noise.

coefficient. The 3 degrees increment between static angle measurements cannot allow a precise estimate of the static stall angle. The latter is predicted between $\alpha_{s,e} = 7.7°$ and $\alpha_{s,e} = 9.7°$ with the correction from Brooks et al. [19], whereas it is predicted between $\alpha_{s,e} = 8.4°$ and $\alpha_{s,e} = 12.4°$ with the correction from Garner et al. [20]. The small values obtained with Brooks' correction reflect the fact that this correction is not accurate for high angles of attack. Comparisons with the lift coefficients obtained with a NACA0012 in another open wind-tunnel at $Re_c = 4.0 \times 10^5$ (see Ref. [23]) and in a closed wind-tunnel at $Re_c = 3.6 \times 10^5$ (see Ref. [24]) shows a good quantitative agreement with current results, confirming that the maximum lift coefficient $C_{l,\max}^{\text{static}}$ obtained in an open wind-tunnel is lower than unity. Further validation of the angle of attack corrections is performed by comparing the measured distribution of static pressure coefficient C_p along the airfoil chord with XFoil simulations. Fig. 2(c) shows an overall good agreement between experiments and XFoil simulations for effective angles of attack estimated thanks to Garner corrections.

Fig. 3 shows the evolution of the PSD of the far-field sound pressure S_{pp} and the PSD of the airfoil surface pressure fluctuations ϕ_{pp} at $x/c = 0.92$ on the suction side for various static angles of attack $\alpha_{s,g}$. For the far-field noise, Fig. 3(a) shows the raw PSD of the sound pressure while Fig. 3(b) presents the PSD of far-field sound pressure with background noise subtracted and data discarded if the total noise does not exceed the background noise by at least 2 dB. For $\alpha_{s,g} = 3°$, the attached turbulent boundary-layer trailing-edge noise is observed: the sound spectrum displays a broadband behavior between 300 Hz and 2000 Hz while the surface pressure PSD is flat with a slight hump centered at 2.5 kHz. The signal to noise ratio is low, with background noise dominating below

300 Hz and above 2 kHz. The increase of the surface pressure PSD at low frequency ($f < 70$ Hz) might be due to a contamination of the spectra by the background noise. For an angle close to stall ($\alpha_{s,g} = 12°$), the far-field noise is increased (+4.5 dB at 500 Hz in comparison with $\alpha_{s,g} = 3°$), which can be attributed to a flow separation on the suction side of the airfoil. This assumption is confirmed by the increase of the amplitude of surface pressure PSD for low frequencies ($f < 2000$ Hz) and the shift of the maximum to a lower frequency ($f = 600$ Hz), indicating an increase of the boundary layer thickness. It is interesting to note that, in spite of the amplitude change, the frequency ranges of the far-field noise for $\alpha_{s,g} = 3°$ and $\alpha_{s,g} = 12°$ are similar.

For the stalled configurations, two regimes are visible, corresponding to the so-called "light-stall" and "deep-stall" regimes [9]. In the light-stall regime ($\alpha_{s,g} = 15°$), a broadband noise is observed between 50 Hz and 700 Hz, with a significant increase at low frequencies (+15 dB at 250 Hz, in comparison with $\alpha_{s,g} = 12°$). The surface pressure PSD exhibits a higher energy content in the low frequencies ($f < 1000$ Hz) than before stall. This high energy in the low frequency range suggests that larger structures are present on the suction side of the airfoil compared to the attached-flow configuration.

The deep-stall regime ($\alpha_{s,g} = 27°$) is characterized by a broadband noise of lower amplitude and a narrow-band peak at 96 Hz. Noise spectra for other high angles of attack not shown here ($\alpha_{s,g} \geq 18°$) all exhibit a peak at $St = 0.21$, where $St = fc\sin(\alpha_{s,g})/U$ being the Strouhal number based on the apparent frontal width of the airfoil. This peak, also noticed on the surface pressure PSD, can be explained by shear layer instabilities and large-scale periodic vortex shedding [9]. At frequencies below and above this peak, the deep-stall regime is less noisy than the light-stall regime, in good agreement with observations by Laratro et al. [12]. Similarly, the surface pressure spectrum level is lower in the deep-stall regime than in the light-stall regime on the entire frequency range. The ratio S_{pp}/ϕ_{pp} is not shown here because the low signal to noise ratio at low angles of attack does not allow conclusive interpretation.

For a fully attached boundary layer, the noise is generated at the trailing-edge of the airfoil [8,26]. In the framework of Amiet's theory, the far-field acoustic pressure PSD S_{pp} is proportional to the surface pressure PSD ϕ_{pp} close to the trailing edge and to the spanwise correlation length l_y [26,27]. As the flow starts separating, the trailing edge is still found to be the main source of noise [9,13]. Surface pressure PSD measured at different positions along the chord are shown in Fig. 4, for various static angles of attack. For comparison with the measurements by Mayer et al. [25] in a Kevlar-walled wind tunnel at $Re = 4\times10^5$, the spectra are normalized by $\rho^2 cU^3$, as suggested by Bertagnolio et al. [2]. For an attached boundary layer ($\alpha_{s,g} = 3°$), similar surface pressure PSD are obtained for the 3 positions along the chord, with a plateau for $1 < fc/U < 3$. However, as the flow separates ($\alpha_{s,g} = 12°$), differences are obvious between the three chord positions. At $x/c = 0.46$, the spectrum still exhibits a plateau with a slight hump at $fc/U = 10$. For positions closer to the trailing-edge, the plateau disappears and the hump amplitude increases while shifting to lower frequencies (at $fc/U = 6$ for $x/c = 0.71$ and at $fc/U = 2.5$ for $x/c = 0.92$). For the light stall regime ($\alpha_{s,g} = 15°$), three regions can be spotted. For $fc/U < 0.8$ and $fc/U > 3$, the surface pressure PSD is higher closer to the trailing edge. On the other hand, for $0.8 < fc/U < 3$, the spectral level are higher closer to the center chord $x/c = 0.46$. Finally, for the deep stall regime ($\alpha_{s,g} = 27°$), the surface pressure PSD is always maximum close to the trailing edge. A good agreement is obtained with closed wind tunnel experiment at $Re = 4\times10^5$ [28], the spectra exhibiting similar slope in the post-stall regimes. The poor magnitude agreement observed in Fig. 4(d) could be explained by the simplistic scaling factor used here and/or by the difference in Reynolds number and angle of attack between the two experimental conditions. According to Bertagnolio et al. [2], using the chord-wise correlation length L_x instead of the chord c could lead to a better collapse of the data. Using a normalized frequency fx_{RMP}/U, with x_{RMP} being the surface pressure probe location, was tested and did not lead to a better collapse of the surface pressure PSD hump center frequencies.

As the surface pressure spectra exhibits close behaviors for the three chord positions and that the amplitude of the surface pressure spectrum is maximum near the trailing edge for the stall condition, only the surface pressure at $x/c = 0.92$ is shown in the following.

3.2. Oscillating-airfoil stall noise

3.2.1. Time–frequency analysis

For the oscillating airfoil regimes, a time–frequency analysis is first performed in order to observe how the surface pressure and far-field noise spectra vary during the oscillation. The spectrograms of the surface pressure and far-field noise for $\alpha_{d,g} = 15° + 7°\sin(2\pi f_o t)$ and $k = 0.02$ are plotted in Fig. 5. The far-field noise and surface pressure fluctuations exhibit strong amplitude variations within an oscillation period. Moreover, the signals of the surface pressure and noise appear to be periodic and strongly in-phase with the instantaneous angle of attack of the airfoil. High values of the angle of attack values are associated with a low-frequency noise contribution. Meanwhile, a high-energy content region appears on the surface pressure spectrogram, with amplitude increases up to +40 dB compared to the attached flow stages.

The frequency content of the spectrum during the stalled stage of the cycle is not uniform. At the stall onset, both the far-field noise and surface pressure present a region of high energy at frequencies up to 1 kHz for a short time interval, whereas the contribution of the remaining part of the stalled stage is limited to frequencies below 1 kHz. As for the static case, the stalled phase exhibits a decrease of the surface pressure level at high frequencies ($f > 1$ kHz) compared to the attached phase, in good agreement with surface pressure spectrograms obtained by Mayer et al. [17] at $x/c = 0.90$. No variations of the far-field noise are visible for $f > 1$ kHz, the frequency range of this quasi-steady stall regime noise is thus similar to the frequency range of the static stall noise.

As results for other oscillation frequencies and amplitudes all exhibit this periodic behavior of far-field noise and surface pressure with respect to the angle of attack, it is possible to apply phase-averaging to microphones and angle of attack signals. Figs. 6 and 7 present the phase-averaged spectrograms for the six oscillating airfoil regimes. In all the following, the overbar denotes phase-averaging. Note on Fig. 6 (g-h-i) and Fig. 7 (g-h-i) that the motion of the airfoil imposed by the motor is not a perfect sinusoidal

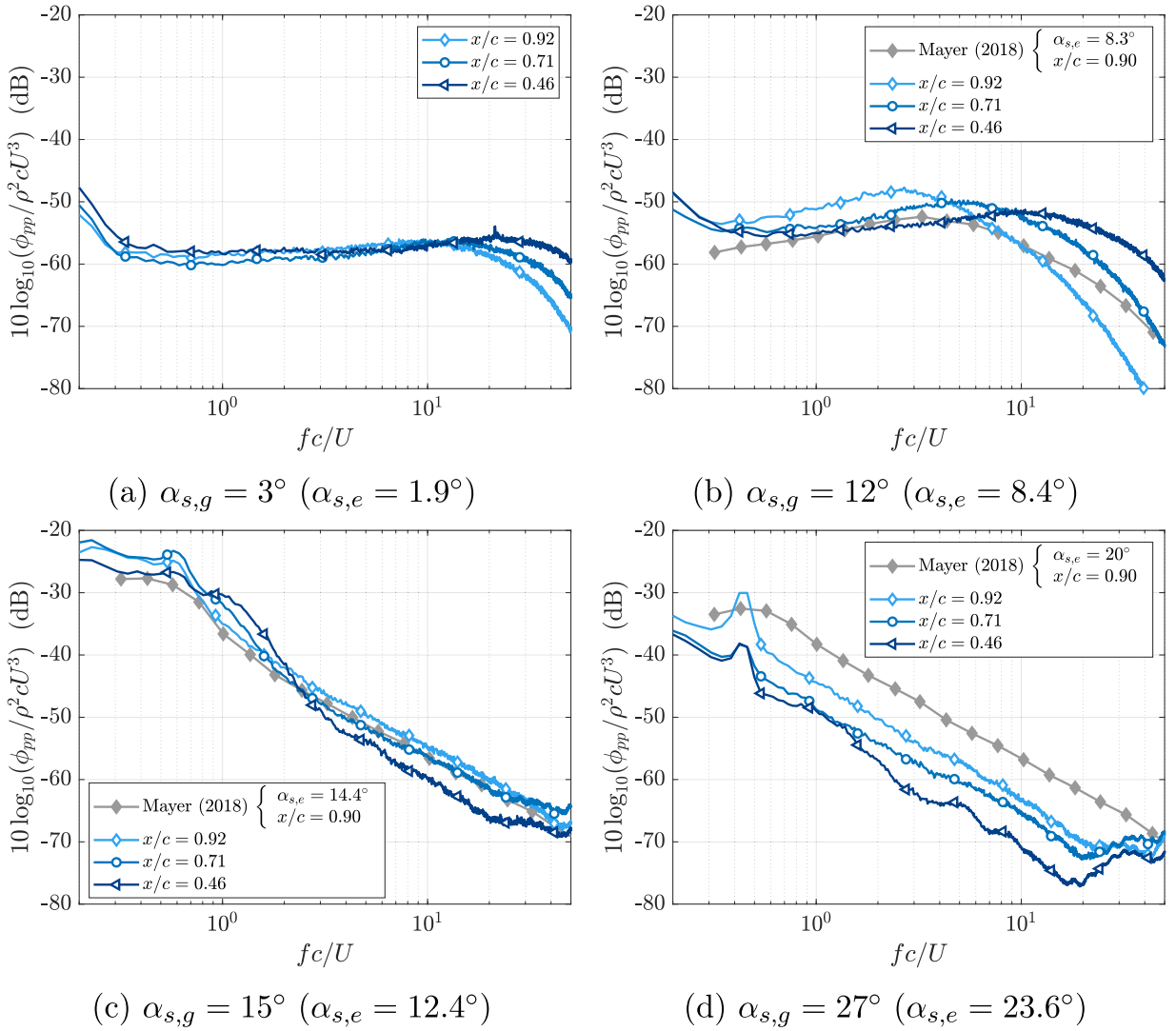

Fig. 4. Comparison of the surface pressure PSD for three positions along the airfoil chord to measurements by Mayer et al. [25] in a Kevlar-walled test section at $Re_c = 4 \times 10^5$ and close static angles of attack.

function. Slight oscillations are evidenced. The total harmonic distortion (THD) of the angle of attack signal was calculated for all the investigated regimes and showed to be less than 20 dB for every amplitude of motion and reduced frequencies. Moreover, a similar experiment was previously performed with a different motor and a different airfoil by Raus et al. [29]. For this experiment, the motor was able to impose a clean sinusoidal motion to the airfoil. Phenomena observed with this experimental setup were similar to the one observed with the current one. These oscillations are thus not believed to be prejudicial for the present time–frequency analysis.

For the quasi-steady regime $\alpha_1 = 7°$ and $k = 0.01$ (left column of Fig. 6), no variation of the noise level is visible outside the stalled stage of the cycle. During the stalled stage, the far-field noise spectrogram is nearly symmetrical. At the onset of stall ($f_0 t \sim 0.30$) and at the flow reattachment time ($f_0 t \sim 0.78$), broadband noise is emitted between 70 Hz and 700 Hz. Between these two moments, the acoustic energy is concentrated in a narrow-band peak centered around $f \simeq 140$ Hz. The light and deep stall regimes observed for a static airfoil are thus still present for an oscillating airfoil in a quasi-steady stall configuration. As for the far-field noise, the surface pressure spectra contain energy at higher frequencies at the stall onset and before flow reattachment than during the stalled stage.

For $\alpha_1 = 15°$ and $k = 0.01$, nearly symmetrical spectrograms are also obtained during the stalled stage for the surface pressure and far-field noise, as seen on the left column of Fig. 7. For this regime, the range of angles of attack during the stalled stage is higher than for $\alpha_1 = 7°$, leading to a visible shift of the narrow-band peak frequency over time on the far-field noise. Just after the stall onset, the narrow-band peak is centered around $f \simeq 145$ Hz. As the angle of attack increases, the center frequency of the

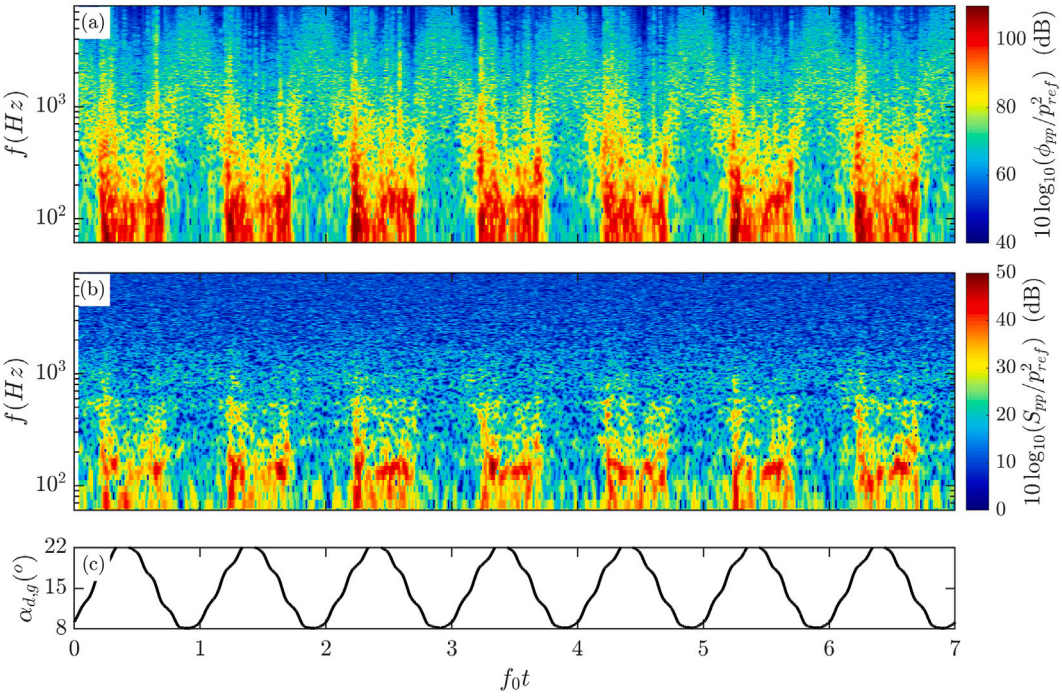

Fig. 5. Spectrograms of (a) surface pressure fluctuations at $x/c = 0.92$ (b) far-field acoustic pressure and (c) instantaneous geometric angle of attack $\alpha_{d,g} = 15° + 7° \sin(2\pi f_o t)$ with $k = 0.02$ ($k_\star = 2.4 \times 10^{-3}$).

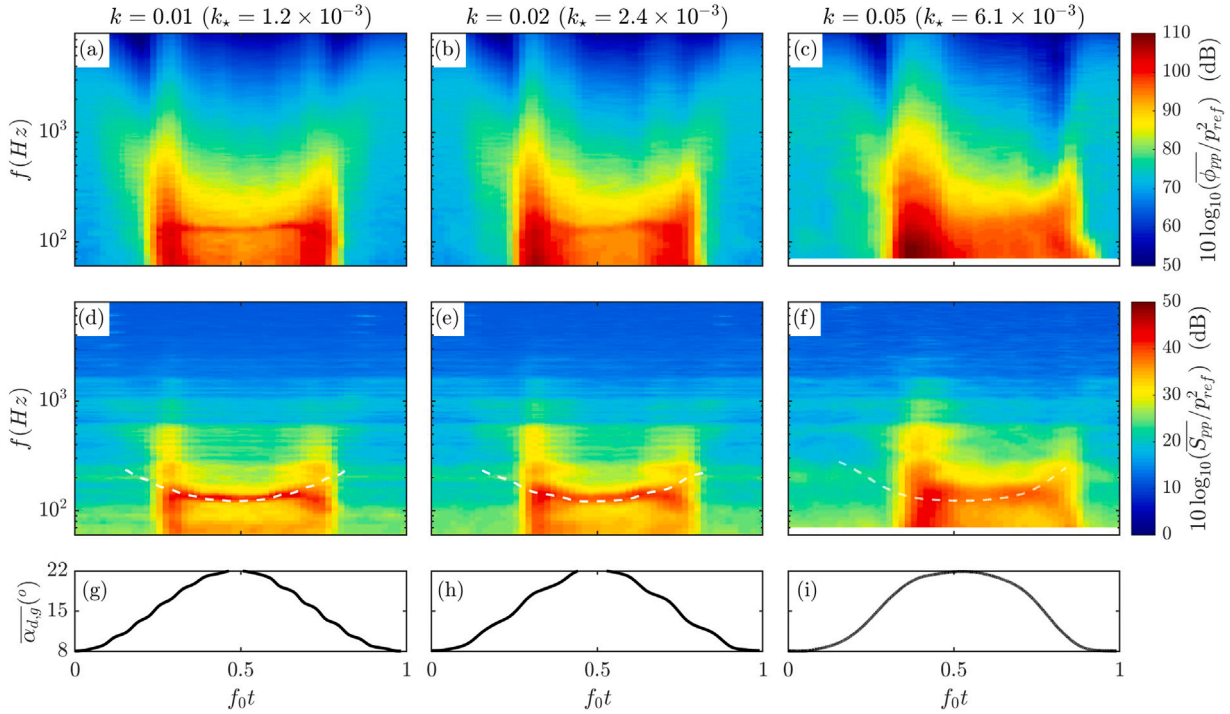

Fig. 6. Phase-averaged spectrograms of (a-b-c) surface pressure fluctuations at $x/c = 0.92$ and (d-e-f) far-field sound pressure, for $\alpha_{d,g} = 15° + 7° \sin(2\pi f_o t)$ and various oscillation frequencies. The third line (g-h-i) shows the phase-averaged variations of angle of attack during one oscillation period. The overbar denotes phase-averaging. The white dashed lines show the evolution of the frequency f corresponding to a constant Strouhal number $St = f c \sin(\overline{\alpha_{d,g}})/U = 0.22$.

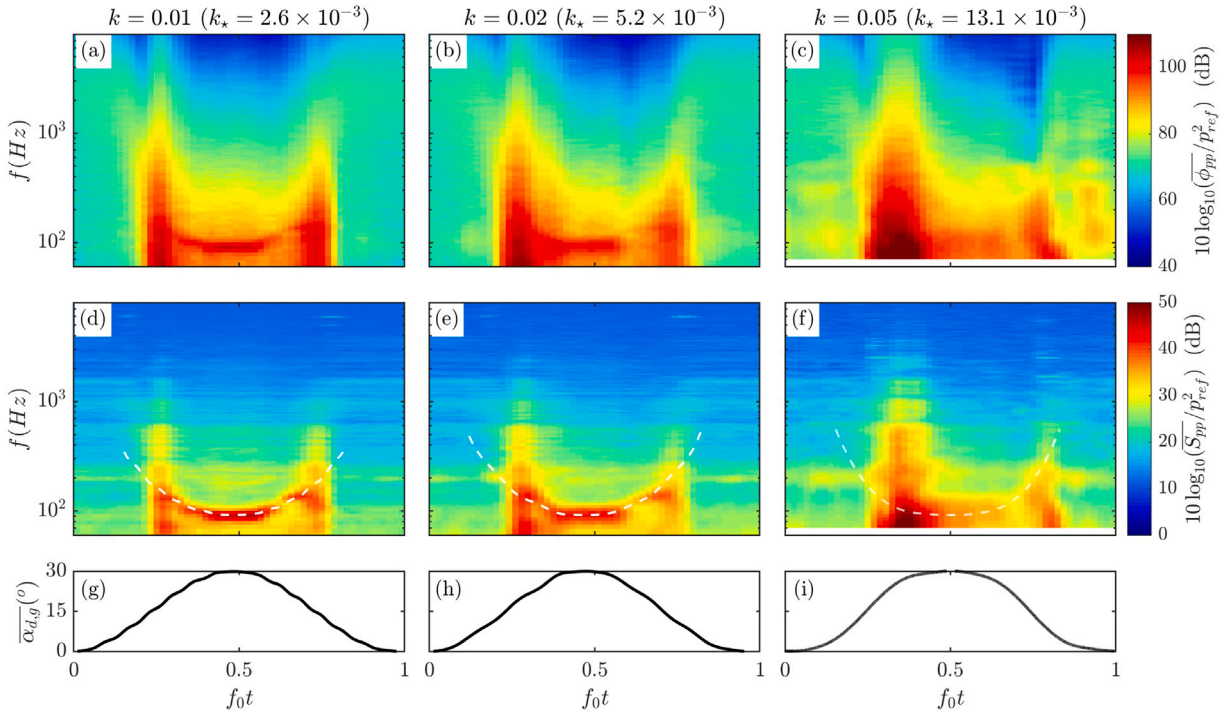

Fig. 7. Same as Fig. 6 with $\alpha_{d,g} = 15° + 15° \sin(2\pi f_o t)$.

peak decreases until reaching a plateau at $f \simeq 94$ Hz, while the airfoil reaches its maximum incidence. The center frequency of the narrow-band peak then starts increasing as the angle of attack decreases, and ends up being centered at $f \simeq 145$ Hz just before the broadband noise at reattachment. This narrow-band peak frequency shift is in good agreement with the static airfoil results, with a Strouhal number $St = fc\sin(\overline{\alpha_{d,g}})/U \simeq 0.22$. During the quasi-steady stall regimes, the sizes of the large structures periodically shed in the flow continuously vary and adapt to the angle of attack of the airfoil. It is noteworthy that, even for the lower reduced frequency $k = 0.01$, the stalled phase is not centered around the maximum of the sinusoidal motion, but is slightly delayed. This phenomenon and the induced hysteresis are investigated in Section 3.2.2.

For $k = 0.02$, similar results are obtained (middle columns of Figs. 6 and 7). However, the symmetrical behavior between stall onset and flow reattachment is lost, the broadband noise at stall onset extending to higher frequencies than the broadband noise at reattachment. This asymmetry is more pronounced for $k = 0.05$ with an increase of the width and amplitude of the stall onset broadband noise. For the dynamic stall regime $k = 0.05$ and $\alpha_1 = 15°$ (see Fig. 7(f)), the stalled stage of the noise cycle does not exhibit any symmetry. The width and amplitude of the broadband noise at stall onset clearly increase, whereas the broadband noise at flow reattachment has a similar length and amplitude compared to the quasi-steady regimes. Note that for $k = 0.05$, the angle of attack signal is slightly distorted, leading to an increased acceleration during the upstroke and downstroke motion of the airfoil. This distortion could have an effect on the dynamic stall noise. However, a similar experiment was conducted by Raus et al. [29] with a NACA$63_3$418 airfoil oscillating in the same open-jet wind tunnel. The motor used for this experiment was able to impose a clean undistorted sinusoidal motion to the airfoil. Phenomena observed with this experimental setup were similar to the ones observed with the present setup. In particular, increasing the reduced frequency of the oscillation also led to an increase of the duration and amplitude of the stall onset broadband noise. The distortion of the angle of attack signal in the present experiment is thus thought to have a limited effect on the stall onset broadband noise modifications observed at higher reduced frequencies.

3.2.2. Overall sound pressure level

In order to further investigate the noise events observed in the spectrograms, a temporal analysis of the dynamic stall noise is conducted by integrating the frequency content of the noise. The Overall Sound Pressure Level (OASPL) is defined as:

$$\text{OASPL} = 10\log_{10}\left(\frac{1}{p_{ref}^2}\int_{f_1}^{f_2} S_{pp}\,df\right), \tag{6}$$

with $p_{\text{ref}} = 20\mu$Pa a reference pressure and $f_1 = 70$ Hz and $f_2 = 1000$ Hz. These values are chosen in order to capture the noise amplitude variations in the stall noise frequency range, as measured in static (Fig. 3) and dynamic (Figs. 6 and 7) configurations, while minimizing the effect of background noise. We then define ΔOASPL = OASPL - $\text{OASPL}_{\alpha_{s,g}=0°}$, with $\text{OASPL}_{\alpha_{s,g}=0°}$ the OASPL value for $\alpha_{s,g} = 0°$. As shown in Fig. 3, background noise dominates below 300 Hz at low angles of attack, for which the boundary

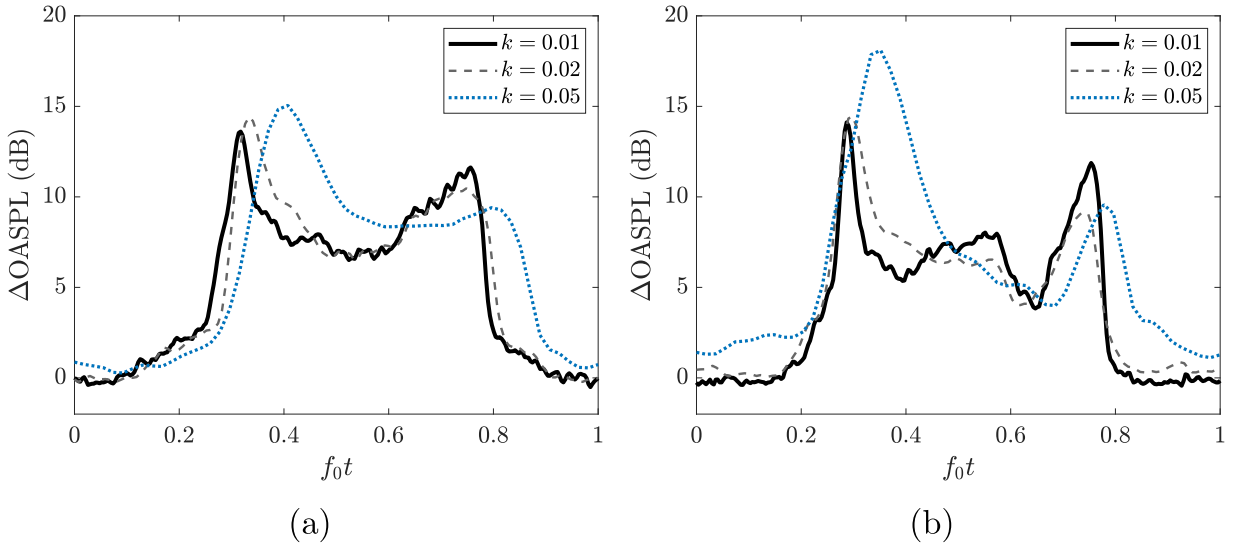

Fig. 8. Phase-averaged ΔOASPL plotted against time for (a) $\alpha_{d,g} = 15° + 7° \sin(2\pi f_o t)$ (b) $\alpha_{d,g} = 15° + 15° \sin(2\pi f_o t)$.

layer is attached. By normalizing OASPL by its value at $\alpha_{s,g} = 0°$, we can calculate the emergence of the noise at low frequency due to the separation of the boundary layer.

The phase-averaged ΔOASPL is plotted against time in Fig. 8, $f_0 t = 0$ corresponding to the minimum value of $\alpha_{d,g}$.

The stalled stage of the noise cycle is characterized by an increase of the noise amplitude by 5 to 15 dB approximately, compared to the attached flow stage. For all the regimes studied here, the ΔOASPL first reaches a maximum value close to the stall onset. It then decreases and reaches a plateau, corresponding to the dynamic deep stall stage observed in Figs. 6 and 7. Finally, the ΔOASPL increases and reaches a second local maximum, marking the onset of flow reattachment, followed by a rapid decrease. For $k = 0.01$, the two local maxima of ΔOASPL have nearly the same value, confirming the aforementioned symmetry, while for higher reduced frequencies, they significantly differ.

In order to compare the aerodynamics of the airfoil and the emitted far-field noise, the ΔOASPL and lift coefficient are both plotted against the angle of attack in Fig. 9 for the static and oscillating airfoil regimes. Note that the static curves are the same and can be used as references for the six dynamic stall experiments. As explained in Section 2.3, steady pressure taps are mainly distributed on one side of the airfoil. In order to calculate C_l for dynamic regimes by integrating the steady pressure along the airfoil, it is therefore necessary to perform measurements for both $\alpha_{d,g} = \alpha_0 + \alpha_1 \sin(2\pi f_o t)$ and $\alpha_{d,g} = -\alpha_0 + \alpha_1 \sin(2\pi f_o t)$, and synchronize the pressure taps during the post-processing phase. This synchronization is a source of error in the estimation of C_l. Moreover, the fact that the motor is not able to generate a perfect sinusoidal motion is also visible on the lift coefficient curves, with slight lift oscillations added to the main lift curve, as seen for example in Figs. 9(d) and 9(j). Again, this artifact is not pronounced enough to question the global analysis of the cycle. The dynamic lift coefficients C_l presented in Fig. 9 have thus to be considered as estimates of the real lift coefficients, with some uncertainty.

Characteristic noise events of the quasi-steady and dynamic stall cycles are numbered from ① to ⑥ and defined in the caption of Fig. 9. Similar noise patterns are obtained for the quasi-steady regimes $k \leq 0.02$, for both $\alpha_1 = 7°$ and 15°. Starting at position ①, the flow is attached and the ΔOASPL for the oscillating airfoil is equal to the one for a static airfoil at the same angle of attack. From position ① to position ②, the angle of attack increases until exceeding the static stall angle but the flow remains attached, the lift coefficient C_l exceeding its maximum static value. From positions ② to ③, the ΔOASPL rapidly increases by more than 10 dB for all the investigated regimes, marking the stall noise radiation, until reaching the maximum ΔOASPL at position ③. Between these two positions, the lift coefficient C_l first reaches its maximum $C_{l,\max}$, before rapidly decreasing. Between positions ③ and ⑤ the flow is fully stalled. A decrease of the ΔOASPL is first visible between positions ③ and ④, as the angle of attack keeps on increasing above the dynamic stall angle. As the angle of attack starts decreasing, the ΔOASPL increases again until reaching a local maximum at position ⑤. The flow reattachment takes place between positions ⑤ and ⑥, where the ΔOASPL decreases rapidly. The angle of attack at the onset of the rapid ΔOASPL increase (position ②) is different from the angle of attack at the rapid ΔOASPL decrease (position ⑥). The hysteresis commonly observed on dynamic lift curves is thus also observed on the ΔOASPL curves. The width of the hysteresis is increasing as the reduced frequency increases. For $k = 0.05$ and $\alpha_1 = 15°$, differences are visible on the ΔOASPL and C_l curves. Unlike for lower oscillation frequencies, the lift coefficient is never decreasing down to $C_l = 0$ when the dynamic angle of attack is low. On the same way, the ΔOASPL for the attached stage of the cycle (between positions ① and ②) is 2 dB higher than the ΔOASPL at the same static angles of attack. For high reduced pitch rates, the trailing edge noise of an attached boundary layer is thus impacted by the pitching motion.

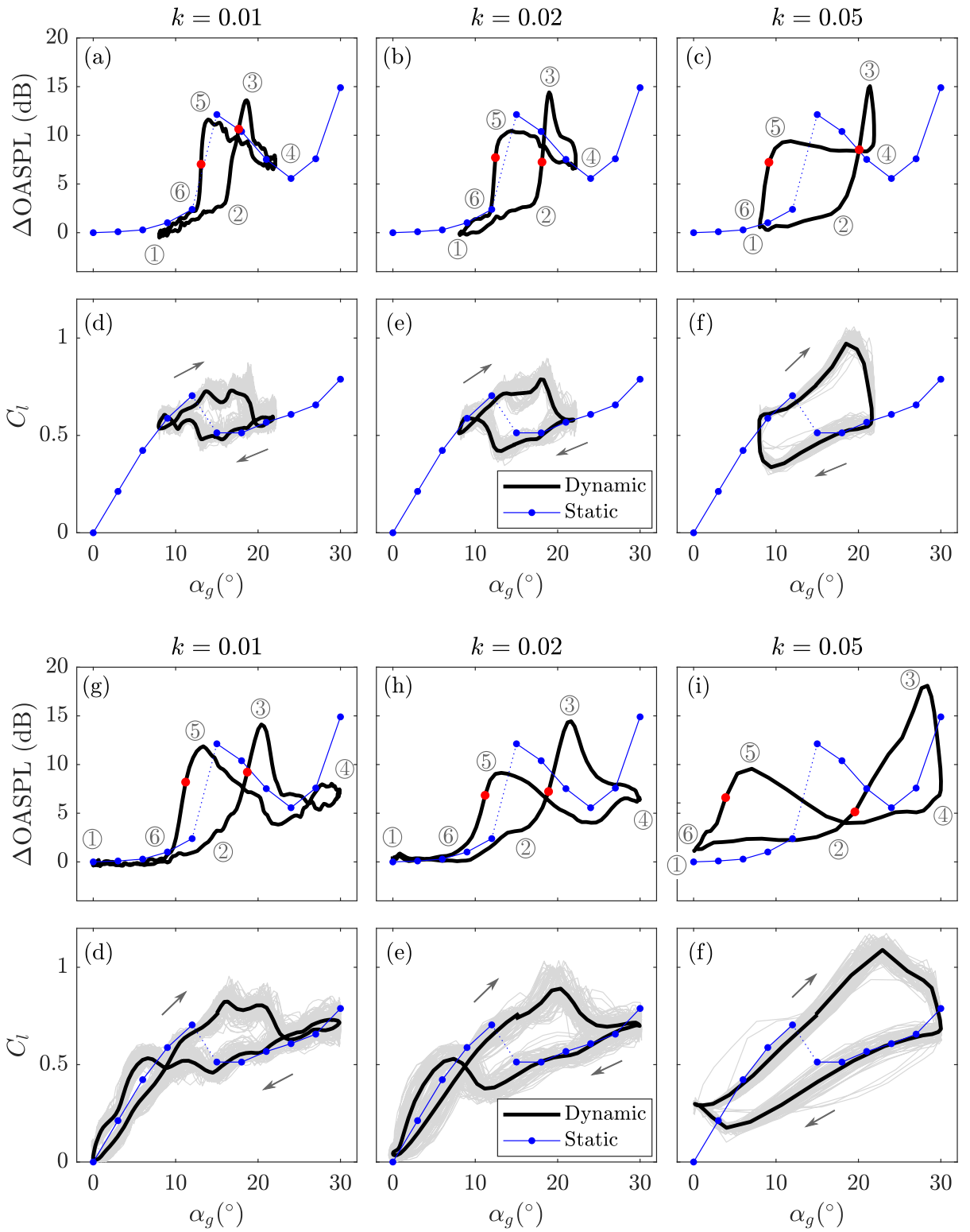

Fig. 9. Phase-averaged Δ OASPL and lift coefficient C_l versus the angle of attack for (a–f) $\alpha_{d,g} = 15° + 7° \sin(2\pi f_o t)$ (g–l) $\alpha_{d,g} = 15° + 15° \sin(2\pi f_o t)$. Gray lines show the instantaneous lift coefficient. Red dots show the angle of maximum dOASPL/dt. α_g here denotes the static or dynamic geometrical angle of attack. Events are defined as: ① Minimum of ΔOASPL and angle of attack, ② Onset of fast ΔOASPL increase, ③ Maximum of ΔOASPL, ④ Maximum of angle of attack, ⑤ Second local maximum of ΔOASPL during downstroke motion and ⑥ End of the rapid ΔOASPL decrease.

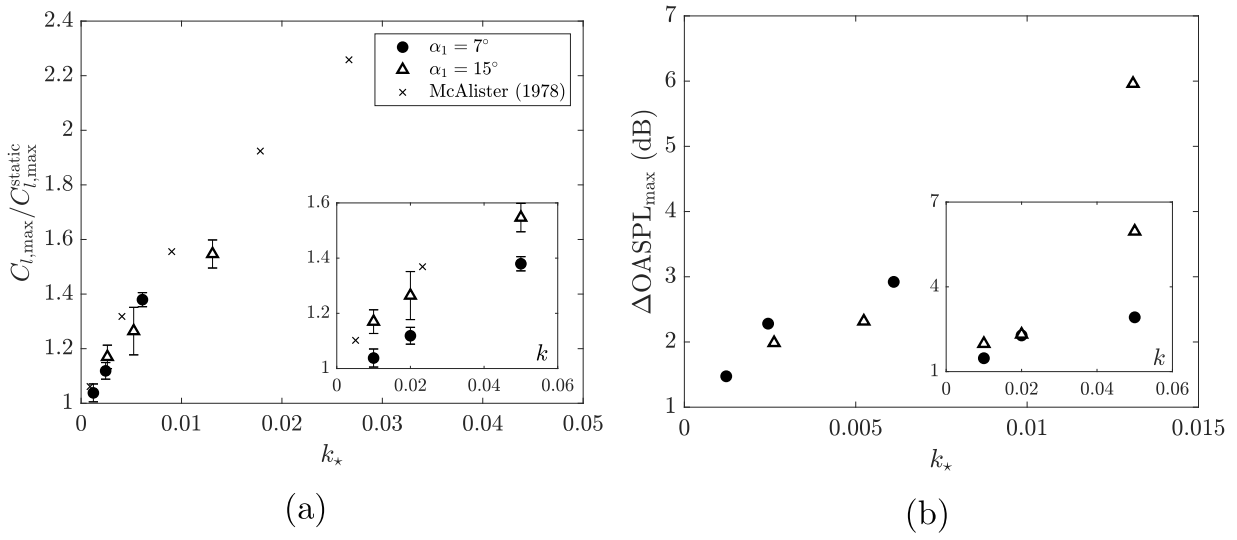

Fig. 10. (a) $C_{l,\max}/C_{l,\max}^{\text{static}}$ and (b) $\Delta\text{OASPL}_{\max}$ versus the reduced pitch rate $k_\star$. Insets show the same data plotted against the reduced frequency k. Filled circles correspond to the $\alpha_{d,g} = 15° + 7° \sin(2\pi f_o t)$ regime, and empty triangles correspond to the $\alpha_{d,g} = 15° + 15° \sin(2\pi f_o t)$ regime.

3.2.3. Lift and noise overshoots

The maximum lift coefficient $C_{l,\max}$ is defined as the maximum of the dynamic lift coefficient curve, located close to the stall onset. The inset of Fig. 10(a) shows the lift overshoot $C_{l,\max}/C_{l,\max}^{\text{static}}$ plotted with respect to the reduced frequency k. Comparison with the measurements of McAlister et al. [4] for a tripped NACA0012 airfoil is performed. McAlister et al. [4] data points are extracted from their Figure 41. As $C_{l,\max}^{\text{static}}$ is not given by authors for tripped experiments, we estimate it as $C_{l,\max}^{\text{static}} \sim 1.35$ by extrapolating $C_{l,\max}$ to $k = 0$. For both $\alpha_1 = 7°$ and $\alpha_1 = 15°$, the lift overshoot increases linearly with k, but the values are higher for $\alpha_1 = 15°$. A better collapse of the data is obtained by plotting the lift overshoot against the reduced pitch rate $k_\star$ in Fig. 10(a). A good agreement is obtained with the measurements of McAlister et al. [4].

As presented above, the dynamic ΔOASPL reaches a maximum close to the stall onset (position ③), before decreasing for higher angles of attack. A far-field noise overshoot can thus be defined as:

$$\Delta\text{OASPL}_{\max} = \text{OASPL}_{\max} - \text{OASPL}_{\max}^{\text{static}}, \tag{7}$$

with $\text{OASPL}_{\max}$ the maximum of the dynamic phase-averaged OASPL and $\text{OASPL}_{\max}^{\text{static}} = 60.7$ dB the maximum of the static OASPL obtained for $\alpha_{s,g} = 15°$. The OASPL overshoot is shown in Fig. 10(b) against the reduced pitch rate $k_\star$ and in the inset of Fig. 10(b) against the reduced frequency k. Once again, a better collapse of the measured data is obtained with $k_\star$. $\Delta\text{OASPL}_{\max}$ increases as the reduced pitch rate increases, with $\Delta\text{OASPL}_{\max} = 1.5$ dB for the quasi-steady regime $k_\star = 1.2 \times 10^{-3}$, and up to $\Delta\text{OASPL}_{\max} = 6.0$ dB for the dynamic stall regime $k_\star = 13.1 \times 10^{-2}$. The oscillating airfoil is thus noisier as its reduced pitch rate increases. Note that the 3° increment between static measurements cannot allow a precise estimate of $\text{OASPL}_{\max}^{\text{static}}$ and $C_{l,\max}^{\text{static}}$.

3.2.4. Dynamic stall angle measurement

It is now investigated if the dynamic stall angle can be measured directly from the far-field noise measurements. Two methods are proposed to measure the dynamic stall angle α_{ds}. Firstly, α_{ds} is estimated as the angle of maximum ΔOASPL, thus corresponding to the ΔOASPL peak observed for every regime close to the stall onset (position ③ in Fig. 9). Secondly, α_{ds} is estimated as the angle of maximum $\text{dOASPL}/\text{d}t$, with $\text{dOASPL}/\text{d}t$ computed with the finite difference method applied to the phase-averaged OASPL signal. This second method provides the angle of attack at which the OASPL increases the fastest. Angles of attack at maximum $\text{dOASPL}/\text{d}t$ are compared in Fig. 11(a) to reference values of stall angles α_{ds} measured on the lift coefficient curves. The reference value of the dynamic stall angle α_{ds} is measured as the angle of maximum lift, as used by Lee and Gerontakos [1]. Values of dynamic stall angles measured on the ΔOASPL curves are compared to the ones measured on the C_l curves in Fig. 11(a). Measuring the maximum $\text{dOASPL}/\text{d}t$ yields a better estimate of the stall angle than measuring the maximum ΔOASPL. The latter tends to overestimate the stall angle.

Sheng et al. [18] show that for dynamic stall experiments with large values of $\alpha_0 + \alpha_1$ compared to α_{ds}, the dynamic stall angle α_{ds} does not depend on the oscillation mean incidence α_0. For this case, the authors obtain a linear increase of α_{ds} with $k_\star$ for $k_\star > 0.01$. They propose the empirical model:

$$\alpha_{ds} = \alpha_{ds0} + \lambda_2 k_\star, \tag{8}$$

for $k_\star > 0.01$, where $\alpha_{ds0} = 18.84°$ and $\lambda_2 = 4.08°$ for a NACA0012 airfoil with an oscillating motion. For $k_\star < 0.01$, Sheng et al. [18] also observe a linear behavior but with a higher slope ($\alpha_{ds} = 15° + 5.95° k_\star$). Fig. 11(b) shows the stall angle α_{ds}, measured on C_l

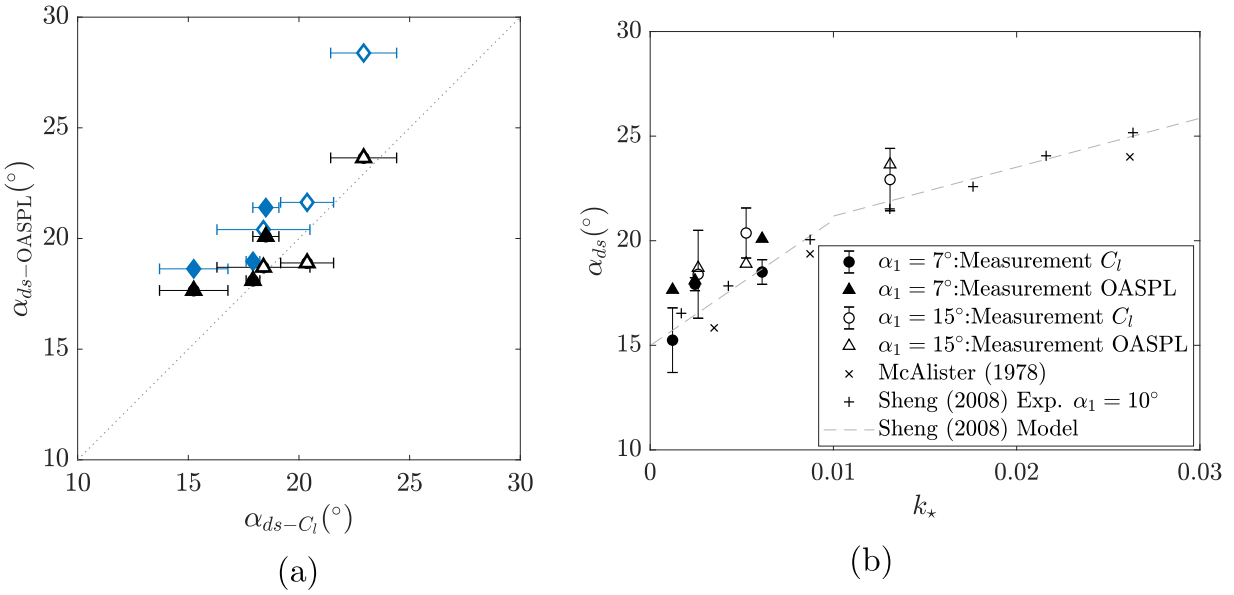

Fig. 11. (a) Comparison between dynamic stall angles $\alpha_{ds-\mathrm{OASPL}}$ estimated from OASPL curves and α_{ds-C_l} estimated from C_l curves. Black triangles correspond to stall angles estimated as maximum dOASPL/dt and blue diamonds correspond to stall angles estimated as maximum of ΔOASPL. Filled symbols correspond to the $\alpha_{d,g} = 15° + 7° \sin(2\pi f_o t)$ regime, and empty symbols correspond to the $\alpha_{d,g} = 15° + 15° \sin(2\pi f_o t)$ regime. (b) Dynamic stall angle versus the reduced pitch rate. (For interpretation of the references to color in this figure legend, the reader is referred to the web version of this article.)

and ΔOASPL curves, versus the reduced pitch rate $k_\star$. In this figure, measurements of α_{ds} from ΔOASPL curves correspond to the angle of maximum dOASPL/dt. The observed slope agrees well with the measurements and empirical model of Sheng et al. [18], and to the measurements of McAlister et al. [4] for a tripped NACA0012 airfoil. Stall angles from the current experiment are higher than the data from Sheng et al. [18] and McAlister et al. [4]. These differences are discussed in Section 4.

3.2.5. *Frequency content of the noise events*

Phase-averaged PSD of the far-field acoustic pressure and surface pressure at the characteristic events ① to ⑤ are extracted from spectrograms and presented in Fig. 12, for $\alpha_{d,g} = 15° + 7° \sin(2\pi f_o t)$. The upward-pointing arrow (↑) indicates the upstroke motion of the airfoil while the downward-pointing arrow (↓) indicates the downstroke motion of the airfoil. Phase-averaged spectra at position ⑥ are not presented in Fig. 12, as they are close to the ones at position ②. Results for $\alpha_{d,g} = 15° + 15° \sin(2\pi f_o t)$ are not shown because they are similar to the ones presented here for $\alpha_{d,g} = 15° + 7° \sin(2\pi f_o t)$.

Starting at $\alpha_{d,g}(t) = 8°$ (position ①) for $k = 0.01$, the far-field noise spectra of Figs. 12(a) and 12(b) display a low amplitude broadband behavior between 300 Hz and 2 kHz. In contrast the surface pressure spectrum is flat with a hump at 2 kHz, as for the trailing-edge noise observed for the static configuration for low angles of attack. As the upstroke motion starts and position ② is reached ($\alpha_{d,g}(t) = 16°(\uparrow)$), the amplitudes of the far-field and surface pressure spectra increase at low frequencies, because the boundary layer is separating on the suction side of the airfoil. This increase continues until reaching the light-stall regime $\alpha_{d,g}(t) = 18.45°(\uparrow)$, corresponding to the angle of maximum OASPL (position ③). As the upstroke motion continues and the maximum incidence is reached ($\alpha_{d,g}(t) = 22°$), a deep-stall type regime is observed, with an overall reduction of the broadband noise and the presence of a peak at $f = 125$ Hz, corresponding to a Strouhal number $St = f c \sin(\alpha_{d,g})/U = 0.22$. The downstroke motion leads to a second light-stall regime at $\alpha_{d,g}(t) = 13.9°(\downarrow)$ (position ⑤). This second light-stall regime is characterized by a broadband noise between 70 Hz and 700 Hz, with lower levels compared to the upstroke light-stall noise from position ③. Similarly, the surface pressure spectrum has a lower amplitude for the downstroke light-stall regime (position ⑤) than for the upstroke light-stall regime (position ③).

Similar results are obtained for $k = 0.02$ and $k = 0.05$ as can be seen in Figs. 12(c) to 12(f). The main effect of increasing the reduced frequency k lays in the noise differences between the upstroke and the downstroke light-stall regimes. For $k = 0.01$, the noise levels in the upstroke and the downstroke light-stall regimes differ by less than 3 dB on the full stall noise frequency range. This difference increases as k increases, with the upstroke light-stall regime being up to 6 dB noisier than the downstroke light-stall regime for $k = 0.05$ (see Fig. 12(f)). Present results do not allow us to investigate if large scale vortex shedding still takes place at $k = 0.05$, because the used window size is too small to study low-frequency narrow-peaks.

3.2.6. *Comparison between the static and quasi-steady stall noise*

A comparison between the quasi-steady stall noise and the static stall noise at similar angles of attack is now performed. Fig. 13 presents the far-field PSD, surface-pressure PSD and steady pressure coefficient C_p distribution for the static regimes $\alpha_{s,g} = 12°$

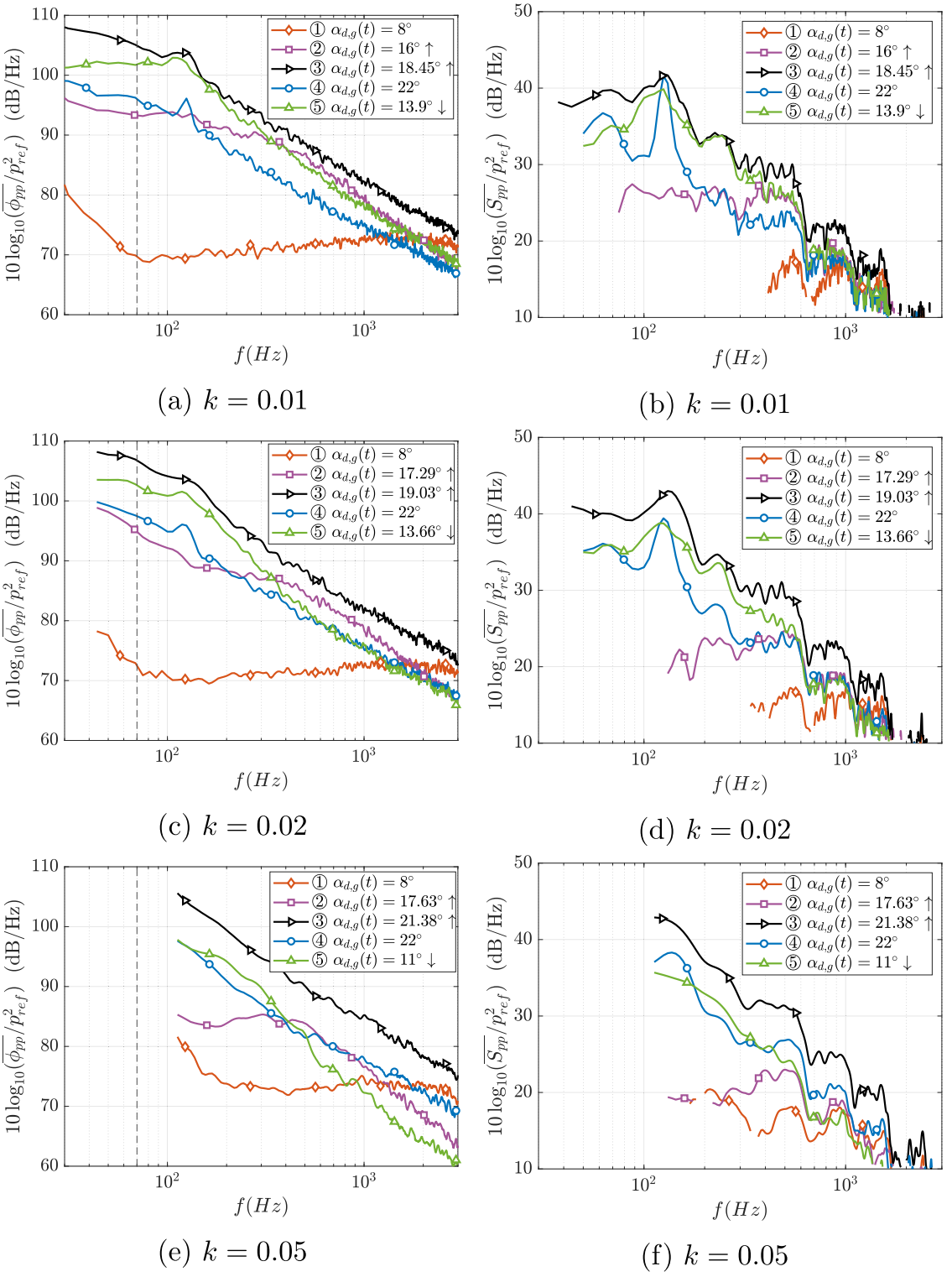

Fig. 12. Phase-averaged PSD of (left column) surface pressure fluctuations at $x/c = 0.92$ and (right column) far-field acoustic pressure with background noise subtracted, during the noise events ① to ⑤ for $\alpha_{d,g} = 15° + 7° \sin(2\pi f_o t)$. The upward-pointing arrow (↑) indicates the upstroke motion of the airfoil while the downward-pointing arrow (↓) indicates the downstroke motion of the airfoil. The vertical dashed black line shows the limit below which the surface pressure spectra is thought to be contaminated by the wind tunnel background noise. Spectra are not displayed at frequencies when less than three points are present per spectrogram window.

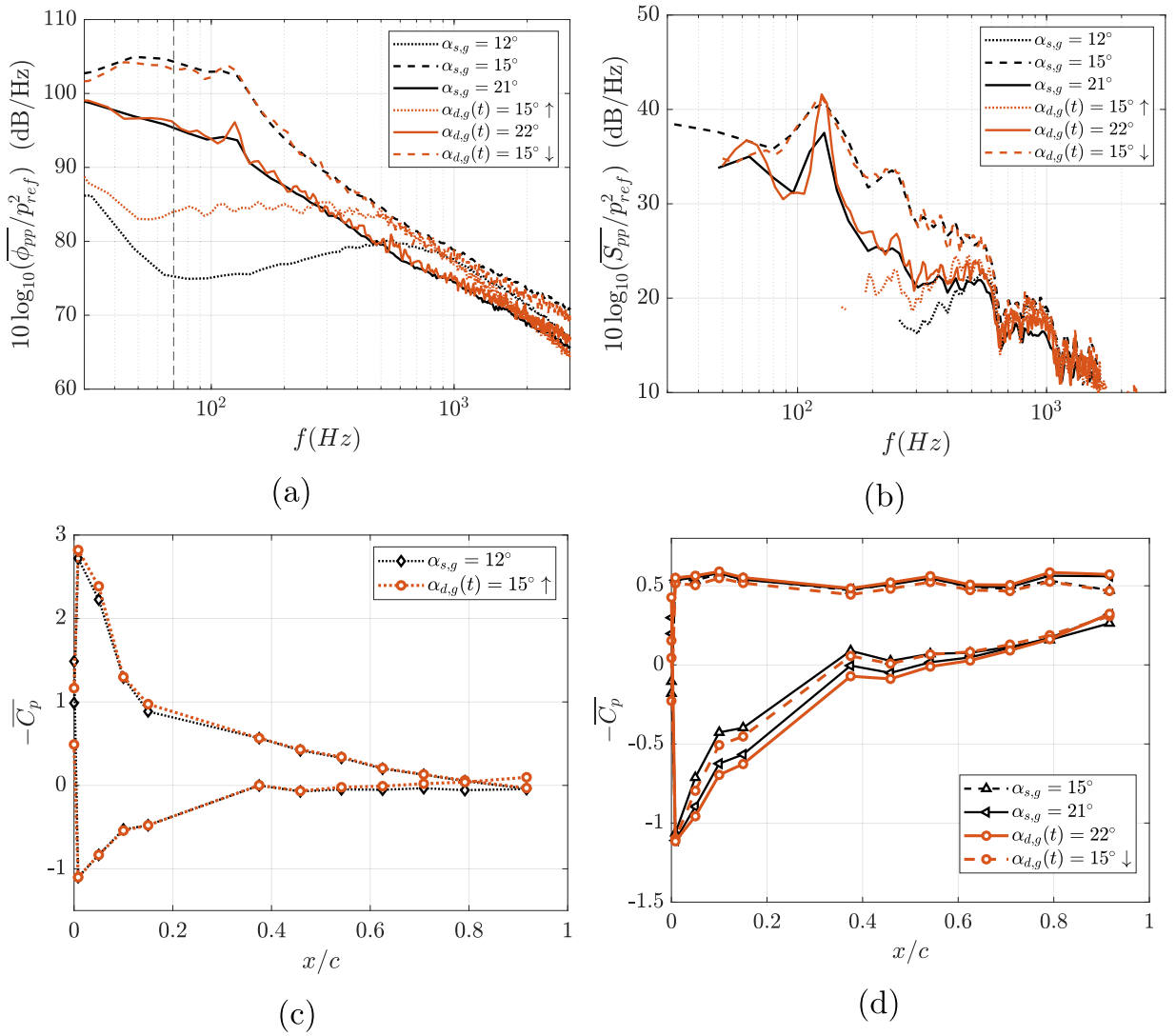

Fig. 13. Comparison of phase-averaged (a) PSD of surface pressure fluctuations at $x/c = 0.92$, (b) PSD of far-field noise and (c–d) static pressure coefficient, between the static and the quasi-steady case $\alpha_{d,g} = 15° + 7° \sin(2\pi f_0 t)$ and $k = 0.01$. Background noise is subtracted from far-field noise and data is discarded if the total noise does not exceeds the background noise by at least 2 dB.

(pre-stall), $\alpha_{s,g} = 15°$ (light-stall) and $\alpha_{s,g} = 21°$ (deep-stall), and for the dynamic regime $\alpha_{d,g} = 15° + 7° \sin(2\pi f_0 t)$ with $k = 0.01$. For a static airfoil, the light-stall noise is observed for $\alpha_{s,g} = 15°$. For the oscillating airfoil, the far-field noise spectrum at $\alpha_{d,g} = 15°(\uparrow)$ still exhibits a pre-stall type shape, with a low amplitude broadband noise limited to frequencies above 200 Hz. This delay of stall during the quasi-steady regime is confirmed by steady pressure measurements, with a steady pressure coefficient distribution similar for $\alpha_{d,g} = 15°(\uparrow)$ and for the static pre-stall regime $\alpha_{s,g} = 12°$ (see Fig. 13(c)). On the other hand, during the downstroke motion, similar far-field and surface pressure spectra are obtained for the static airfoil at $\alpha_{s,g} = 15°$ and for the oscillating airfoil at $\alpha_{d,g} = 15°(\downarrow)$. This result confirms that a hysteresis is present for the emitted noise, even for the quasi-steady regime with the lowest oscillation frequency investigated. The noise emitted by the quasi-steady oscillating airfoil can thus be predicted thanks to static noise measurements, and by adding an angle of attack delay that can be calculated using a dynamic stall model.

4. Discussion

The maximum values of ΔOASPL at stall onset and flow reattachment observed for the quasi-steady regimes are in good agreement with the static measurements of Lacagnina et al. [13]. According to the authors, the static stall noise can originate from the interaction between the shear layer and the suction side of the airfoil. At the critical angles of attack (stall onset or flow reattachment), the shear layer is the closest to the airfoil, leading to a strong interaction and maximum noise radiation. This

can explain the maxima of ΔOASPL near the stall onset and flow reattachment observed in Fig. 8. For higher angles of attack, the distance between the shear layer and the suction side increases. As the hydrodynamic pressure generated in the shear layer decreases exponentially with distance, the interaction between the shear layer and the suction side of the airfoil reduces, and less noise is generated. This can explain the broadband noise amplitude decrease during the "deep-stall" stage of the cycle.

On the one hand, the fact that the ΔOASPL is nearly symmetrical between stall onset and flow reattachment for the quasi-steady regimes can be explained by the interpretation of Lacagnina et al. [13]. On the other hand, as observed on spectrograms and ΔOASPL curves, the transition to the dynamic stall regime ($k = 0.05$ and $\alpha_1 = 15°$) leads to a symmetry breaking between stall onset and flow reattachment that cannot be explained by this static interpretation. Aerodynamic investigations of the dynamic stall phenomenon show that the main difference between static and dynamic stall happens during the stall development and at the stall onset, with the development and detachment of the large-scale dynamic stall vortex [7]. The passage of this dynamic stall vortex above the suction side of the airfoil is known to modify the surface pressure distribution on the airfoil [1]. Moreover, Fig. 10 shows a correlation between the aerodynamics of the airfoil and the far-field emitted noise, with the commonly observed lift overshoot associated with a noise overshoot. For dynamic stall regimes, the lift overshoot is known to be partly due to the low pressure region created as the dynamic stall vortex is convected above the suction side of the airfoil [6]. Further measurements are thus needed in order to determine if this dynamic stall vortex is the cause of the strong increase of $\Delta\text{OASPL}_{\text{max}}$ for the dynamic stall regime.

Measurements of the dynamic stall angle α_{ds} from OASPL curves show a good agreement with measurements from lift coefficient curves as seen in Fig. 11(b). Stall angles in the current experiment are larger than those of McAlister et al. [4] and Sheng et al. [18]. Two hypotheses could explain this difference. Firstly, Sheng et al. [18] experiments are conducted in a closed wind-tunnel, whereas the current experiments are conducted in an open-jet one. For static configurations, the deflection of the flow in an open-jet wind-tunnel is known to delay stall to higher angles [19], as already explained in Section 2.3. A similar effect is expected for dynamic configurations. Secondly, unlike the experiments of Sheng et al. [18] where the airfoil is oscillating about its quarter chord point, it was chosen here to make the airfoil oscillates about its mid-chord point, in order to minimize the deflection of the jet by the airfoil at high incidence. The effect of the pitch location on dynamic stall was investigated by Jumper et al. [30] for a NACA0015 with ramp-up motion. The authors show that shifting the pitch location from $c/4$ to $c/2$ also leads to delaying the dynamic stall to higher angles of attack.

5. Conclusion

Aeroacoustic measurements of the dynamic stall of an oscillating NACA0012 airfoil at Reynolds number $Re_c = 2.1 \times 10^5$ are conducted in an open-jet anechoic wind tunnel. The effect of the reduced pitch rate $k_\star = \alpha_1 k$ of the oscillation on the emitted noise is studied thanks to simultaneous far-field and surface pressure measurements.

Until now, stall noise models for wind turbines were implemented for static airfoils [2], while the present paper shows that even at moderate reduced frequency, the noise emitted by an oscillating airfoil can substantially differ from the one for a static airfoil. The results in the present paper imply the incapacity of static airfoil noise models to describe the noise emitted by an airfoil undergoing dynamic stall. This experiment confirms that the amplitude and frequency of the oscillation have an effect on the amplitude and duration of the emitted stall noise. For all the reduced pitch rates investigated, the stall noise takes place as the airfoil incidence increases over the critical dynamic stall angle α_{ds}. This stall noise is characterized by an increase of the relative Overall Sound Pressure Level (ΔOASPL) by more than 10 dB compared to the trailing-edge noise emitted during the attached boundary-layer stage of the pitching cycle.

A quasi-steady behavior is obtained for a low reduced pitch rate ($k_\star = 1.2 \times 10^{-3}$), where the light-stall and deep-stall regimes commonly observed for a static airfoil are retrieved. The time–frequency analysis of the emitted noise reveals a symmetrical behavior of the quasi-steady stall noise pattern, similar light-stall type noises being observed at the stall onset and before flow reattachment. These regimes are characterized by a low frequency broadband noise between 70 Hz and 700 Hz. Between these events, the deep-stall regime is obtained, with a reduction of the low-frequency broadband noise and the apparition of a narrow-band peak at a Strouhal number $St = fc\sin(\alpha_{s,g})/U = 0.22$, the frequency of the bluff body large scale vortex shedding adapting to the instantaneous angle of attack of the airfoil. The ΔOASPL appeared to be maximum at the stall onset and before flow reattachment. For the dynamic stall regime at higher $k_\star$ ($k_\star = 13.1 \times 10^{-3}$), the acoustic signatures at stall onset and flow reattachment are not similar, with an increase of the amplitude and duration of the stall onset noise. This increase could be explained by the development of the dynamic stall vortex on the suction side of the airfoil. An overshoot of maximum ΔOASPL is observed and increases with the reduced pitch rate $k_\star$. Measurements of stall angles are performed by detecting the angles of maximum of $d\text{OASPL}/dt$. Good agreement with measurements from lift coefficient curves is obtained. Even for the quasi-steady regimes, a delay in the presence of the stall noise is observed in comparison with the static stall noise, leading to a hysteresis of the stall noise as a function of the angle of attack. This hysteresis width increases as the reduced pitch rate increases. In the future, similar measurements will be performed with a NACA63_3418 airfoil, a thick and cambered airfoil typically used on wind turbines blades. For this airfoil, synchronized acoustic and time-resolved Particle Image Velocimetry (PIV) measurements will be conducted, in order to understand the role of the flow structures around the airfoil on the sound generation mechanisms.

CRediT authorship contribution statement

David Raus: Investigation, Formal analysis, Writing – original draft, Visualization. **Benjamin Cotté:** Conceptualization, Investigation, Formal analysis, Writing – review & editing. **Romain Monchaux:** Conceptualization, Investigation, Formal analysis, Writing – review & editing. **Emmanuel Jondeau:** Methodology, Investigation, Resources, Validation. **Pascal Souchotte:** Methodology, Investigation, Resources, Validation. **Michel Roger:** Conceptualization, Investigation, Formal analysis, Writing – review & editing.

Declaration of competing interest

The authors declare that they have no known competing financial interests or personal relationships that could have appeared to influence the work reported in this paper.

Acknowledgments

This research is funded by the French National Agency for Research under grant agreement N°ANR-18-CE04-0011 and by the Agence Innovation Défense under grant agreement N°2018 60 0071 00 470 75 01.

References

[1] T. Lee, P. Gerontakos, Investigation of flow over an oscillating airfoil, J. Fluid Mech. 512 (2004) 313–341.
[2] F. Bertagnolio, H. Madsen, A. Fischer, C. Bak, A semi-empirical airfoil stall noise model based on surface pressure measurements, J. Sound Vib. 387 (2016).
[3] A.-J. Buchner, J. Soria, D. Honnery, A.J. Smits, Dynamic stall in vertical axis wind turbines: scaling and topological considerations, J. Fluid Mech. 841 (2018) 746–766.
[4] K. McAlister, L. Carr, W. McCroskey, U.S.N. Aeronautics, S. Administration, Dynamic stall experiments on the NACA0012 airfoil, in: NASA technical paper, National Aeronautics and Space Administration, Scientific and Technical Information Office, 1978.
[5] L.W. Carr, Progress in analysis and prediction of dynamic stall, J. Aircr. 25 (1) (1988) 6–17.
[6] T. Corke, F. Thomas, Dynamic stall in pitching airfoils: Aerodynamic damping and compressibility effects, Annu. Rev. Fluid Mech. 47 (2015).
[7] K. Mulleners, M. Raffel, Dynamic stall development, Exp. Fluids 54 (2) (2013) 1469.
[8] T.F. Brooks, D. Pope, M. Marcolini, Airfoil self-noise and prediction, in: NASA Reference Publication 1218, 1989.
[9] S. Moreau, M. Roger, J. Christophe, Flow features and self-noise of airfoils near stall or in stall, in: 15th AIAA/CEAS Aeroacoustics Conference (30th AIAA Aeroacoustics Conference), 2009.
[10] S. Oerlemans, Effect of wind shear on amplitude modulation of wind turbine noise, Int. J. Aeroacoustics 14 (5–6) (2015) 715–728.
[11] J. Turner, J. Kim, Aerofoil dipole noise due to flow separation and stall at a low Reynolds number, Int. J. Heat Fluid Flow 86 (2020) 108715.
[12] A. Laratro, M. Arjomandi, B. Cazzolato, R. Kelso, Self-noise and directivity of simple airfoils during stall: An experimental comparison, Appl. Acoust. 127 (2017) 133–146.
[13] G. Lacagnina, P. Chaitanya, T. Berk, J.-H. Kim, P. Joseph, B. Ganapathisubramani, S.M. Hasheminejad, T.P. Chong, O. Stalnov, K.-S. Choi, M.F. Shahab, M. Omidyeganeh, A. Pinelli, Mechanisms of airfoil noise near stall conditions, Phys. Rev. Fluids 4 (2019) 123902.
[14] A. Manela, On the acoustic radiation of a pitching airfoil, Phys. Fluids 25 (7) (2013) 071906.
[15] T. Zhou, Y. Sun, R. Fattah, X. Zhang, X. Huang, An experimental study of trailing edge noise from a pitching airfoil, J. Acoust. Soc. Am. 145 (4) (2019) 2009–2021.
[16] L. Siegel, K. Ehrenfried, C. Wagner, K. Mulleners, A. Henning, Cross-correlation analysis of synchronized PIV and microphone measurements of an oscillating airfoil, J. Vis. 21 (3) (2018) 381–395.
[17] Y. Mayer, B. Zang, M. Azarpeyvand, Aeroacoustic investigation of an oscillating airfoil in the pre- and post-stall regime, Aerosp. Sci. Technol. 103 (2020) 105880.
[18] W. Sheng, R.A.M. Galbraith, F.N. Coton, Prediction of dynamic stall onset for oscillatory low-speed airfoils, J. Fluids Eng. 130 (10) (2008).
[19] T.F. Brooks, M. Marcolini, D. Pope, Airfoil trailing edge flow measurements and comparison with theory, incorporating open wind tunnel corrections, in: 9th Aeroacoustics Conference, 1984.
[20] H.C. Garner, E. Rogers, W. Acum, E. Maskell, Subsonic Wind Tunnel Wall Corrections, Tech. rep., AGARDograph, 1966.
[21] G. Yakhina, Experimental Study of the Tonal Trailing-Edge Noise Generated by Low-Reynolds Number Airfoils and Comparison with Numerical Simulations, (Ph.D. thesis), Ecole Centrale de Lyon, Lyon, 2017.
[22] P. Welch, The use of fast Fourier transform for the estimation of power spectra: a method based on time averaging over short, modified periodograms, IEEE Trans. Audio Electroacoust. 15 (2) (1967) 70–73.
[23] Y. Mayer, B. Zang, M. Azarpeyvand, Design of a kevlar-walled test section with dynamic turntable and aeroacoustic investigation of an oscillating airfoil, in: 25th AIAA/CEAS Aeroacoustics Conference, 2019.
[24] R.E. Sheldahl, P.C. Klimas, Aerodynamic characteristics of seven symmetrical airfoil sections through 180-degree angle of attack for use in aerodynamic analysis of vertical axis wind turbines, http://dx.doi.org/10.2172/6548367, URL https://www.osti.gov/biblio/6548367.
[25] Y. Mayer, B. Zang, M. Azarpeyvand, Design of a kevlar-walled test section with dynamic turntable and aeroacoustic investigation of an oscillating airfoil, in: 25th AIAA/CEAS Aeroacoustics Conference, 2018, http://dx.doi.org/10.2514/6.2019-2464.
[26] R. Amiet, Noise due to turbulent flow past a trailing edge, J. Sound Vib. 47 (3) (1976) 387–393.
[27] M. Roger, S. Moreau, Extensions and limitations of analytical airfoil broadband noise models, Int. J. Aeroacoustics 9 (3) (2010) 273–305.
[28] Y. Mayer, B. Zang, M. Azarpeyvand, Aeroacoustic characteristics of a NACA0012 airfoil for attached and stalled flow conditions, in: 25th AIAA/CEAS Aeroacoustics Conference, 2019.
[29] D. Raus, L. Sicard, B. Cotté, R. Monchaux, E. Jondeau, P. Souchotte, M. Roger, Experimental characterization of the noise generated by an airfoil oscillating above stall, in: AIAA AVIATION 2021 FORUM, American Institute of Aeronautics and Astronautics, VIRTUAL EVENT, United States, 2021.
[30] E.J. Jumper, R.L. Dimmick, A.J.S. Allaire, The effect of pitch location on dynamic stall, J. Fluids Eng. 111 (3) (1989) 256–262.